Publication Year	2022
Acceptance in OA	2025-03-07T15:05:33Z
Title	The Giant Magellan Telescope Natural Guidestar Adaptive Optics mode: improving the robustness of segment piston control
Authors	Quirós-Pacheco, Fernando, van Dam, Marcos, Bouchez, Antonin H., Conan, Rodolphe, Haffert, Sebastiaan Y., AGAPITO, Guido, Demers, Richard
Publisher's version (DOI)	10.1117/12.2629618
Handle	http://hdl.handle.net/20.500.12386/36529
Serie	proceedings of spie
Volume	12185

The Giant Magellan Telescope natural guidestar adaptive optics mode: improving the robustness of segment piston control

Fernando Quirós-Pacheco, Marcos van Dam, Antonin Bouchez, Rodolphe Conan, Sebastiaan Haffert, et al.

Fernando Quirós-Pacheco, Marcos van Dam, Antonin H. Bouchez, Rodolphe Conan, Sebastiaan Y. Haffert, Guido Agapito, Richard Demers, "The Giant Magellan Telescope natural guidestar adaptive optics mode: improving the robustness of segment piston control," Proc. SPIE 12185, Adaptive Optics Systems VIII, 1218517 (29 August 2022); doi: 10.1117/12.2629618

Event: SPIE Astronomical Telescopes + Instrumentation, 2022, Montréal, Québec, Canada

The Giant Magellan Telescope Natural Guidestar Adaptive Optics mode: improving the robustness of segment piston control

Fernando Quirós-Pacheco*[a], Marcos van Dam[b], Antonin H. Bouchez[a], Rodolphe Conan[a],
Sebastiaan Y. Haffert[c], Guido Agapito[d], and Richard Demers[a]
[a]GMTO Organization, 465 North Halstead St, Suite 250, Pasadena, CA 91107, USA,
[b]Flat Wavefronts, 21 Lascelles Street, Christchurch 8022, New Zealand,
[c]University of Arizona, Steward Observatory, Tucson, Arizona, USA,
[d]Osservatorio Astrofisico di Arcetri (INAF), Largo E. Fermi 5, I-50125 Firenze, Italy.

ABSTRACT

The Natural Guidestar Adaptive Optics (NGAO) system of the Giant Magellan Telescope (GMT) uses a visible-light modulated pyramid wavefront sensor (PWFS) to measure the wavefront aberrations, including residual segment piston errors. This paper presents an updated wavefront sensing and control architecture that increases the robustness of segment piston control. In the first place, the Natural Guide star Wavefront Sensor (NGWS) design has been updated to incorporate the recently proposed Holographic Dispersed Fringe Sensor (HDFS) as a second wavefront sensing channel measuring unambiguously differential segment piston errors as large as ~14 microns. In the second place, an optimized modal control strategy has been developed to compensate mode-by-mode for the optical gain of the PWFS. We report on the simulated NGAO performance results obtained when using a R=12 guide star, and with a turbulence strength of r_0 =12.8 cm.

Keywords: Giant Magellan Telescope, Extremely Large Telescopes, co-phasing, adaptive optics, wavefront control, pyramid wavefront sensor, dispersed fringe sensor, modal control optimization.

1. THE GMT NGAO MODE

The GMT[1] is a 25.4m doubly-segmented Gregorian telescope, with a primary mirror (M1) composed of seven circular 8.4m segments, and an Adaptive Secondary Mirror (ASM) with matching segmentation. In the NGAO mode, the ASM will provide a Single Conjugate Adaptive Optics (SCAO) correction that will enable high resolution, high-contrast imaging in the infrared, and improve the wavelength stability of high-resolution single-object spectrographs[2,3]. Wavefront sensing will be performed by the Natural Guidestar Wavefront Sensor (NGWS) unit using the visible light reflected off a dichroic instrument window.

The NGWS must sense all wavefront error caused by the atmosphere and telescope, including image motion and segment phase piston error. The need to sense segment phase piston at high bandwidth drove the selection of a modulated pyramid wavefront sensor (PWFS), which also provides high sensitivity and low aliasing. Because the PWFS is blind to segment piston errors consisting of an integer number of waves, a second wavefront sensing channel is used to measure these phase wrapping errors. The NGWS design presented at the preliminary design review[4] featured a second PWFS operating in a narrowband with a central wavelength different from the main PWFS channel that allowed to infer segment wrapping errors of up to three waves. The NGWS design has been recently modified to incorporate the novel Holographic Dispersed Fringe Sensor (HDFS)[5] that can unambiguously measure segment phase piston errors as large as ~14 microns. A summary of the main parameters of the two NGWS wavefront sensing channels is presented in Table 1. The details of the HDFS simulation are presented in Section 2.

*fquiros@gmto.org; phone +1 626 204-0543; www.gmto.org

Adaptive Optics Systems VIII, edited by Laura Schreiber, Dirk Schmidt, Elise Vernet,
Proc. of SPIE Vol. 12185, 1218517 · © 2022 SPIE
0277-786X · doi: 10.1117/12.2629618

Table 1. Summary of main parameters of the NGWS wavefront sensing channels.

NGWS **1st Channel** **(PWFS)**	**Sensing band:** ▪ 600 – 920 nm (central wavelength: $\lambda_1 = 760$ nm). ▪ 90% of NGWS light in this band used by the 1st channel. **Spatial sampling:** ▪ Pupil sampled by a grid of 92×92 sub-apertures (SA) across the GMT diameter. ▪ Given the particular GMT pupil, the number of valid SA (i.e. sufficiently illuminated) is $n_{vs} \leq 6000$. **Signal processing:** ▪ Slopes computation method. ▪ Size of PWFS measurement vector ($\mathbf{s_1}$): $n_{sig} = 2 \cdot n_{vs} \leq 12000$ **Tilt modulation:** ▪ Circular modulation synchronized with detector's readout. ▪ Nominal modulation radius: $\theta_{mod} = 2\,\lambda_1/D$ **Detector parameters (EMCCD):** ▪ Selected camera: First Light OCAM^{2}K ▪ Detector size: 240×240 pixels ▪ Readout noise: <1.0 e^- RMS at the fastest readout ▪ Excess noise factor: √2 ▪ Frame rate: $f_{AO} \leq 2$ kHz ▪ Average quantum efficiency in sensing band: 0.890
NGWS **2nd channel** **(HDFS)**	**Sensing band:** ▪ 700 – 920 nm (wavelength for mean wavenumber: $\lambda_2 = 795$ nm). ▪ 10% of NGWS light in this band used by the 2nd channel. **Spatial Filter:** ▪ 40 mas in diameter **Fringe imaging parameters:** ▪ Pixel scale: 2.40 mas ▪ FoV enclosing all fringes: 1400×1400 mas (583×583 pixels) ▪ size of HDFS measurement vector ($\mathbf{s_2}$): 14 ▪ Sub-aperture (SA) size (i.e. extracted fringe box): 187×187 mas (78×78 pixels) **Detector parameters (EMCCD):** ▪ Selected camera: Princeton ProEM-HS 1024BX3 ▪ Detector size: 1024×1024 pixels ▪ Readout noise: <1.0 e^- RMS ▪ Dark current: <0.002 e^-/s ▪ Excess noise factor: √2 ▪ Frame rate: $f_P = 5 - 50$ Hz ▪ Average quantum efficiency in sensing band: 0.732

The wavefront control strategy in the NGAO mode has been recently revised to incorporate an on-sky modal optimization strategy known as the Modal Gain Machine (MGM)[6]. The simplified NGAO control loop diagram is shown in Figure 1. There are two aspects of the MGM that need to work in unison. In the first place, an Optical Gain Tracking Loop (OGTL) compensating for the sensitivity loss of the PWFS in the partial AO correction regime. In the second place, an on-line optimization of the temporal controller parameters to cope with changes in the observing conditions (e.g. seeing, guide star flux level, etc.). In our current NGAO simulations, the temporal controller is an Optimized Modal Gain Integrator (OMGI). Hence, the MGM ensures that the AO closed-loop stability is not compromised when both optical gain compensation coefficients and OMGI gains are updated simultaneously. The details of our MGM implementation are presented in Section 3.

The simulated performance of the PWFS+HDFS wavefront sensing and control architecture is presented in Section 4.

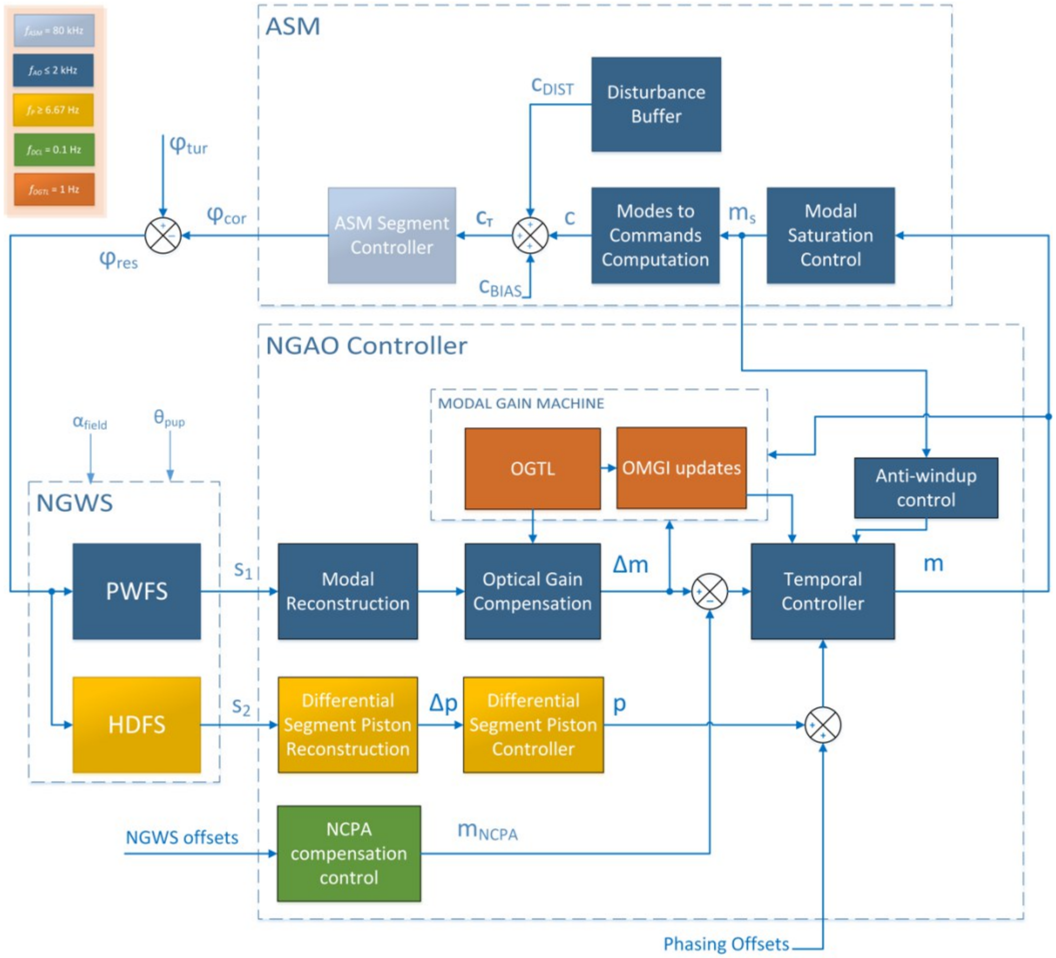

Figure 1. Simplified NGAO control loop diagram.

2. SEGMENT PISTON CONTROL WITH THE HDFS

In this section we describe how we plan to use the HDFS as a second NGWS wavefront sensing channel. A schematic representation of the HDFS channel is shown in Figure 2. The HDFS uses a binary phase mask ($\pm\pi/2$ rad) to interfere and disperse light from selected segment pairs of the GMT onto different locations in the focal plane (see Figure 3). As described in Haffert et al.[5], the binary hologram defined over each segment represents two multiplexed grating patterns that selectively interfere each segment with two others (see Table 2). In the focal plane, each grating creates two dispersed fringe patterns on either side of the optical axis; one for the $m = 1$ diffraction order and one for the $m = -1$. The binary hologram has a high efficiency because most of the light (~80%) is concentrated into the $m = \pm 1$ diffraction order.

The HDFS phase mask can be manufactured to be chromatic or achromatic. Achromatic phase masks can be more efficient as they minimize the crosstalk between the zeroth and the first orders[5] but are more difficult to manufacture. Chromatic phase masks can be manufactured with conventional etching techniques.

On the left of Figure 3 we show the HDFS phase mask designed by S. Haffert and used in all our simulations. We have assumed that the phase mask is chromatic and defined for the mean wavenumber of the sensing band: $\lambda_2 = 795$ nm (c.f. Table 1). On the right of Figure 3 we show the dispersed fringes in the focal plane for a flat reference wavefront. As reported in Table 2, three different baselines (i.e. center-to-center distance) between interfered segments give rise to three distinct groups of fringes.

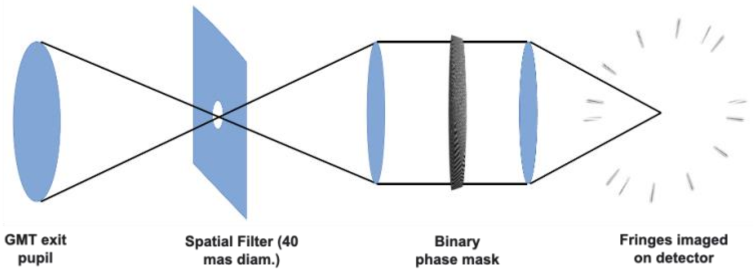

Figure 2. Schematic representation of the HDFS. The light is passed through a field stop, then collimated, passed through the binary phase mask, and imaged onto a detector.

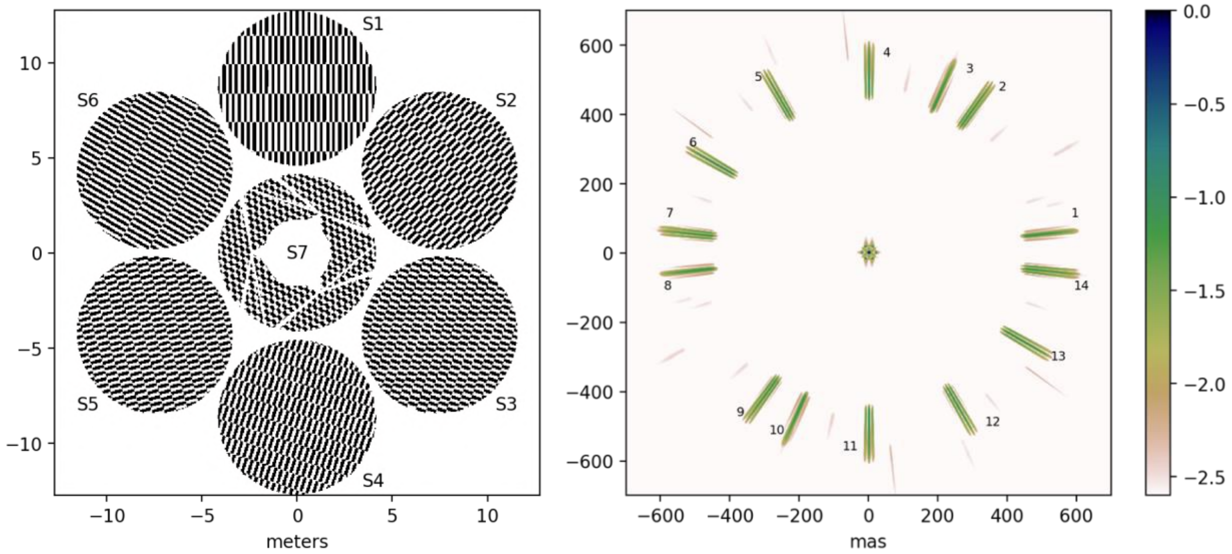

Figure 3. (**Left**) HDFS binary phase mask with $+\pi/2$ and $-\pi/2$ radians of phase difference shown in black and white, respectively. The GMT pupil mask has been applied for visualization purposes, and the GMT segment ID numbers are also shown. (**Right**) Dispersed fringes produced in the focal plane for a flat reference wavefront. The image size is 1.4×1.4 arcsec and contains the zeroth and the first diffraction orders (log scaled intensities). The fringes ID numbers are also shown.

Table 2. Summary of relationship between pairs of interfered GMT segments and the fringes produced and shown in Figure 3. The baseline (i.e. center to center distance) between pairs of segments is also reported.

Fringe IDs ($m = \pm 1$ diffraction order)	1, 8	2, 9	3, 10	4, 11	5, 12	6, 13	7, 14
Interfered segment pairs	S1–S7	S6–S3	S7–S6	S3–S5	S5–S2	S2–S4	S4–S1
Baseline [m]	8.71	17.42	8.71	15.09	17.42	15.09	17.42

Contribution	Throughput
HDFS chromatic mask efficiency (estimated relative flux in first orders)	0.8036
Spatial filter (40 mas in diameter)	0.8689
ProEM QE (averaged in HDFS sensing band)	0.7323
Total	0.5113

Table 3. HDFS efficiency estimation in diffraction-limited conditions.

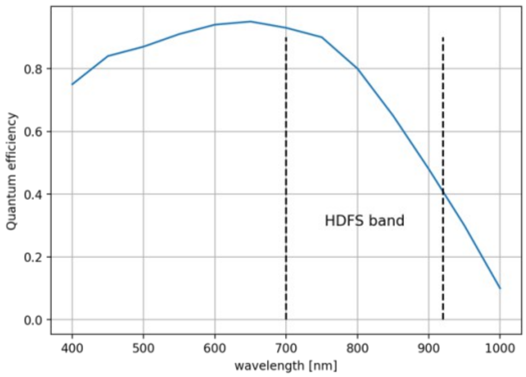

Figure 4. Quantum efficiency curve of the selected Princenton ProEM-HS camera for the HDFS.

Table 3 reports an estimation of the HDFS efficiency in diffraction-limited conditions. We should note that 3% of the light is lost to the zeroth order as a combined effect of the chromatic mask efficiency and the spatial filter. As we will show in Section 4, the spatial filter will cause the throughput to be much lower in the presence of residual turbulence.

2.1 From fringes to segment piston estimates

In this section we describe how to convert the HDFS fringes into segment piston estimates. The processing is illustrated in Figure 5 and Figure 6. The first task is to extract the fringes from the full frame like the one shown on the right of Figure 3. The location of the fringes is a-priori known from the design of the HDFS mask. An oversized box around the center of each fringe is defined, and the fringes are extracted and derotated so that they are all vertical with the longest wavelength at the top. The size of the box is then reduced to 78×78 pixels (187×187 mas) for further processing. We will abuse the AO language and refer to these extracted boxes as *HDFS sub-apertures*, with the same numbering as the fringe IDs.

The fringes are then apodized to remove any cross-contamination from one sub-aperture to another, and to avoid spectral leakage when we take the FFT of the fringes. A good apodization function will gently force the value of the image to zero near the edges while minimizing the destruction of information in the image. While the optimal form of apodization is not known for our application, we have successfully used a Tukey apodization function in all our simulations, as shown in Figure 7(a).

The next step is based on the DFS processing used in the GMT Acquisition, Guiding and Wavefront Sensing (AGWS) units that has been shown to work using numerical simulations as well as tests in the laboratory and on the Magellan telescope.[7,8] First, we take the absolute value of the Fourier transform of the derotated and apodized fringes (Figure 6). The absolute value of the Fourier transform is known as the Fourier amplitude. Then, for each Fourier amplitude, we extract the values of pixels around the peak of the sidelobe (whose a-priori separation from the central lobe is given by the baseline between the interfered GMT segments). The two sidelobes are exactly symmetric so we only need to consider one sidelobe. Finally, we use quadratic interpolation to find the subpixel location of the peak. The quadratic interpolation is performed along the x-axis and then along the y-axis. The vector containing the 14 estimated y-ordinates of the sidelobe peaks defines the HDFS measurement vector, and we denote it as $\mathbf{s_2}$.

Following the processing pipeline described above, we can then calibrate an interaction matrix ($\boldsymbol{D_2}$) between the GMT segment piston values and the HDFS using the classical push-pull approach. The resulting 14×7 interaction matrix is shown in Figure 7(b). The HDFS segment piston reconstruction matrix is computed as the regularized least-squares of the interaction matrix:

$$\boldsymbol{R_P} = \left[\boldsymbol{D_2^T C_{nn}^{-1} D_2} + \boldsymbol{\beta J}\right]^{-1} \boldsymbol{D_2 C_{nn}^{-1}} \tag{1}$$

where $\boldsymbol{C_{nn}}$ is the HDFS measurement noise covariance matrix, $\boldsymbol{\beta}$ is a large constant, and $\boldsymbol{J}$ is a matrix of ones required to penalize global piston. Finally, the differential segment piston ($\mathbf{\Delta p}$) estimated from HDFS measurements ($\mathbf{s_2}$) is computed as:

$$\mathbf{\Delta p} = \boldsymbol{R_P}(\mathbf{s_2} - \mathbf{s_{2,ref}}) \tag{2}$$

where $\mathbf{s}_{2,\mathbf{ref}}$ is the HDFS reference measurement vector computed from a flat wavefront (see Figure 5).

As shown in the block diagram of Figure 1, the HDFS segment piston estimate is passed on to a differential piston controller that determines whether a phase-wrapping error (aka segment ejection) has occurred. This controller basically compares the absolute value of the 7 elements of $\mathbf{\Delta p}$ with a threshold value (set to $0.8\lambda_1$ in our simulations). The output of the controller is a 7-element vector ($\mathbf{p}$) that only includes the piston values that exceed the threshold.

2.2 Capture range evaluation

Figure 7(c) shows the capture range in diffraction-limited conditions of the HDFS. We have pushed one GMT segment at a time and reconstructed the segment piston vector from HDFS measurements. We note that segments S1 and S6 have the lowest capture range (~11 μm WF). This is because these segments are associated with the fringes produced by the shortest baselines, as reported in Table 2. The capture range for other segments is ~14 μm WF.

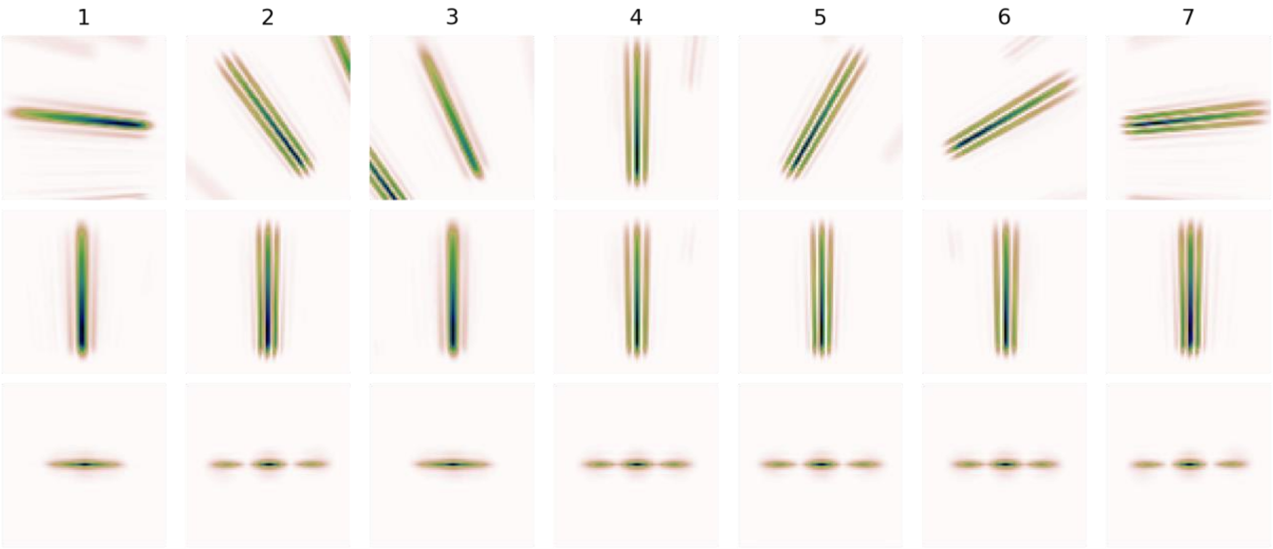

Figure 5. Diffraction-limited and noiseless fringes produced by a flat wavefront. Only the first 7 fringes are shown (i.e. $m = +1$ diffraction orders). (**Top**) Raw extracted fringes. (**Middle**) Derotated and apodized fringes. (**Bottom**) Fourier amplitudes. The HDFS measurement vector computed from these Fourier amplitudes is the HDFS reference vector ($\mathbf{s}_{2,\mathbf{ref}}$).

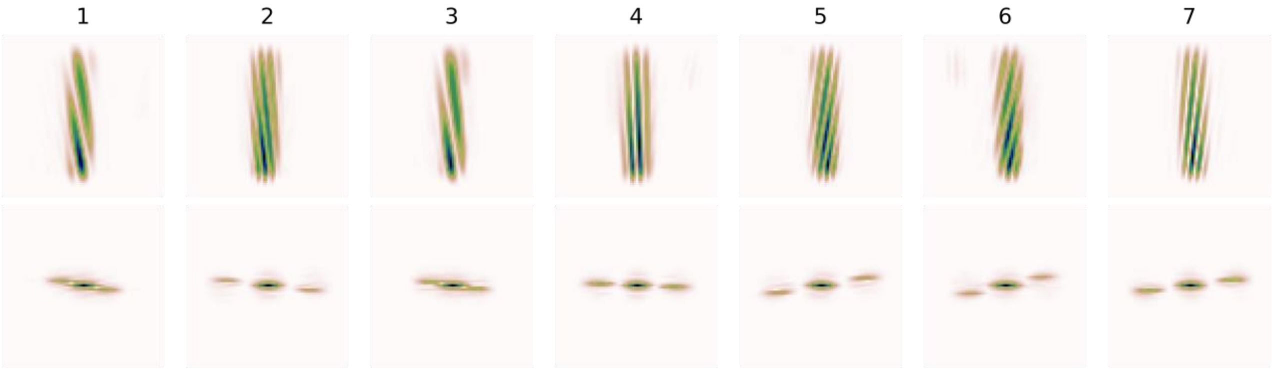

Figure 6. Diffraction-limited and noiseless fringes produced by a random segment piston error of 3 μm WF RMS. Only the first 7 fringes are shown (i.e. $m = +1$ diffraction orders). (**Top**) Derotated and apodized fringes. (**Bottom**) Fourier amplitudes. The HDFS measurement vector ($\mathbf{s}_2$) is computed from these Fourier amplitudes.

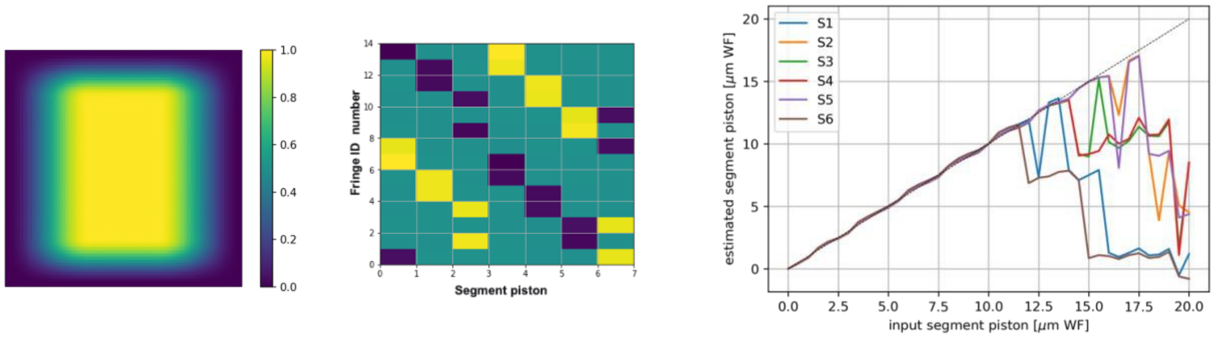

(a) (b) (c)

Figure 7. **(a)** Apodization function generated with two one-dimensional Tukey (tapered cosine) functions with different values of the cosine fraction. **(b)** Interaction matrix between segment piston values and HDFS measurements. **(c)** Evaluation of the capture range of the HDFS by pushing one GMT segment at a time.

3. MODAL GAIN MACHINE

In this section we describe the optimized modal control (aka Modal Gain Machine[6]) that we have recently developed for the GMT NGAO system. This approach has allowed us to increase the robustness of segment piston control. In the first place, we have chosen to define the AO modes over each segment rather than over the whole GMT pupil. Taking advantage of the ASM segmentation, the segment modes are Karhunen-Loeve (KL) modes fitted by the ASM segment influence functions. While the modal basis for the outer segments (S1 to S6) is the same, for the central segment (S7) we must consider the central obscuration in the modal basis definition (obscuration caused by the M2 baffle of 3.5 m in diameter).

It is important to note that the seven segment piston modes are by construction members of the segment KL basis, orthogonal to all other modes, and so they can be controlled independently in our modal control scheme. The sections below describe our implementation of the Modal Gain Machine (MGM).

3.1 Optical gain tracking loop

It is now well understood in the AO community that pyramid-based AO systems need to compensate for the sensitivity changes of the PWFS (aka optical gain) affecting the on-sky performance as the observing conditions evolve. Our method is based on the Optical Gain Tracking Loop (OGTL) described in Esposito et al.[9] which requires the injection of a small probe signal and a demodulation analysis to estimate the optical gain. We describe our implementation below which has some important customizations.

The purpose of our OGTL is to find the set of optical gain compensation (OGC) coefficients that restore the diffraction-limited sensitivity of the PWFS. Assuming that the optical gains between modes are decoupled, the restored (or effective) optical gain of the i-th mode at iteration k is:

$$\gamma_i^{eff}(k) \triangleq \gamma_i(k) \cdot \mathscr{k}_i(k) \tag{3}$$

where γ_i denotes the real (and unknown) optical gain of the PWFS, and $\mathscr{k}_i$ is the OGC coefficient we seek to find. If we knew the value of γ_i we would simply set $\mathscr{k}_i(k) = \gamma_i^{-1}$. In practice, the OGC coefficients are found iteratively, and when the OGTL converges, the "effective" optical gains of all modes tend to one ($\gamma_i^{eff} \approx 1$). We can rewrite equation (3) in a way that it can be used for iterative estimations of the optical gains as:

$$\hat{\gamma}_i(k) = \hat{\gamma}_i(k-1) / \gamma_i^{eff}(k) \tag{4}$$

and linearize it in the form[10] $\gamma_{new} = \gamma_{old} + \epsilon(\gamma_{old})$ so that the update is performed with a numerical integrator of gain g_{OGTL} applied to the increment function $\epsilon(\gamma_{old})$:

$$\hat{\gamma}_i(k) = \hat{\gamma}_i(k-1) + g_{OGTL}\left[\hat{\gamma}_i(k-1) \cdot \left[\gamma_i^{eff}(k) - 1\right]\right]. \tag{5}$$

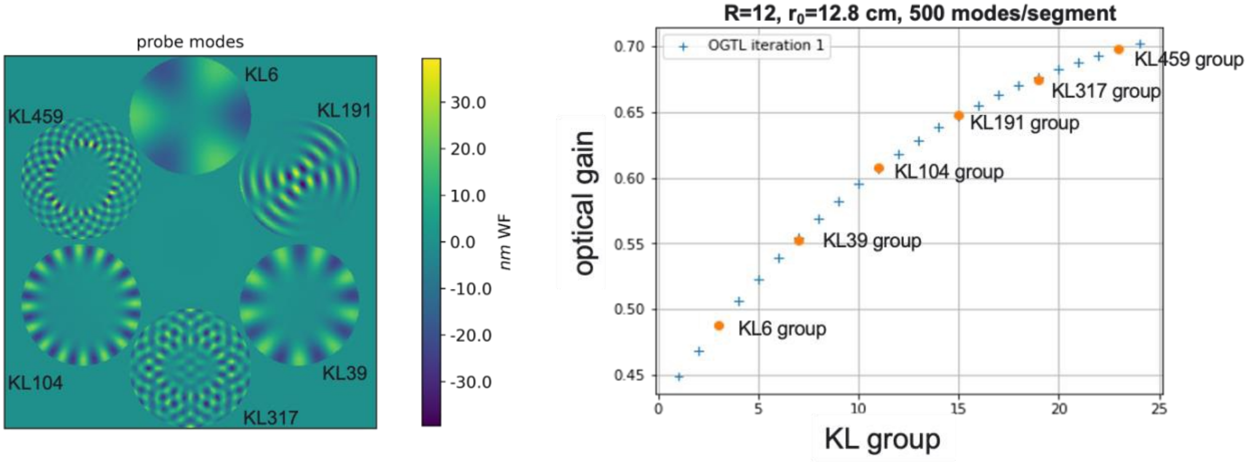

Figure 8. **(Left)** Probe modes modulated on each outer segment with an amplitude of 10 nm RMS WF. **(Right)** Example of optical gain interpolation for all KL groups using the optical gains estimated on the probe modes.

In practice, we can only attempt to probe a subset of modes. Taking advantage of our segment KL basis, we chose to sinusoidally modulate a probe mode per outer segment with a small amplitude (10 nm RMS WF) and with a high frequency (210 Hz). The probe modes are shown in Figure 8. The probe commands are preloaded on a dedicated ASM "disturbance buffer" shown in the block diagram of Figure 1.

The *effective* optical gains of our set of probe modes $\{\gamma_l^{eff}\}$ can be estimated by demodulation of both the residual modal command vector ($\mathbf{\Delta m}$) and the modal command vector $(\mathbf{m})$ as:

$$\gamma_l^{eff}(k) = \frac{\mathcal{D}\left\{\Delta m_l(n)_{1\le n\le N_{OGTL}}\right\}}{\mathcal{D}\left\{m_l(n)_{1\le n\le N_{OGTL}}\right\}}, \tag{6}$$

where $\mathcal{D}\{\cdot\}$ denotes the demodulator operator. The subscript notation $1 \le n \le N_{OGTL}$ denotes a collected time history made of N_{OGTL} samples; n denotes the discrete time at which the main AO loop is updating (every 1 ms in our simulations), and k denotes the discrete time at which MGM is updating (every 1s in our simulations).

Equations (5) and (6) allow us to estimate the optical gains of the probe modes $\{\hat{\gamma}_l\}$. Now we need a method to estimate the optical gains for the rest of the modes. In our simulations, $\mathrm{n_{mode}}$=3500 segment KL modes (i.e. 500 modes/segment). Modes with similar "radial order" (i.e. spatial frequency content) experience the same optical gain. Hence, we clustered our 3500 segment KL modes in 24 KL groups with similar radial order. This allowed us to estimate the optical gain of all KL groups by interpolating a cubic polynomial to the optical gain values estimated for the probes (c.f. Figure 8).

Once the optical gains of all modes have been estimated $\{\gamma_i\}$, the OGC coefficients $\{\mathscr{k}_i\}$ are simply computed as:

$$\mathbf{K_{OGC}} \triangleq \begin{bmatrix} \mathscr{k}_1 & \cdots & 0 \\ \vdots & \ddots & \vdots \\ 0 & \cdots & \mathscr{k}_{\mathrm{n_{mode}}} \end{bmatrix} = \begin{bmatrix} \gamma_1^{-1} & \cdots & 0 \\ \vdots & \ddots & \vdots \\ 0 & \cdots & \gamma_{\mathrm{n_{mode}}}^{-1} \end{bmatrix}, \tag{7}$$

and the residual modal command vector is then computed with the updated $\mathbf{K_{OGC}}$ as:

$$\mathbf{\Delta m}(n) = \mathbf{K_{OGC}}\boldsymbol{R_1}\boldsymbol{s_1}(n)\ . \tag{8}$$

3.2 OMGI gains update

The procedure to update the integral gains of an Optimized Modal Gain Integrator (OMGI) is well known. Recall that the ultimate purpose is to adjust the bandwidth of the temporal controller to cope with changes in the observing conditions (e.g. seeing, guide star flux level, etc.). The same data stream needed for the OGTL (i.e. delta commands $\mathbf{\Delta m}$ and integrated commands $\mathbf{m}$, as shown in the block diagram of Figure 1) is used to reconstruct the "open-loop" commands time series ($\mathbf{m^{OL}}$). The optimized modal gains $\{\hat{g}_i\}$ are then found by minimizing the Dessenne criterion[11]:

$$J_i = \int_{-\infty}^{\infty} |E_i(j\omega)|^2 \left\langle \left|\tilde{m}_i^{OL}(j\omega)\right|^2 \right\rangle d\omega \tag{9}$$

where E_i is the rejection transfer function (RTF) of the i-th mode, which is a function of the modal gain g_i. The operator $\langle|\cdot|^2\rangle$ represents the temporal Power Spectral Density (PSD), and $\omega = 2\pi f_{AO}$. The parameters of the RTF need to be characterized in advance (notably the total delay of the AO loop).

The modal gains $\{g_i\}$ and the OGC coefficients $\{\mathscr{k}_i\}$ are updated at the same time in the MGM scheme[6]. To avoid abrupt changes in the controller, the modal gains are low-pass filtered ($\rho = 0.5$) and scaled by the gain changes that will be introduced by the OGTL:

$$g_i(k) = \left[[1-\rho]\, g_i(k-1) + \rho \hat{g}_i(k)\right] \cdot \frac{\mathscr{k}_i(k-1)}{\mathscr{k}_i(k)} \tag{10}$$

where k denotes the discrete time at which MGM is updating (every 1s in our simulations).

4. PERFORMANCE SIMULATIONS

We present in this section simulation results obtained with the CUDA-Engined Optics (CEO)[12] tool, which is the fast raytracing and wavefront propagator toolbox that forms part of the GMT Integrated Model. We have implemented the HDFS and PWFS models in this framework, to run efficiently with GPU acceleration. The full end-to-end NGAO system simulation is coded in Python interacting with the Python interface of CEO with the aid of the CuPy library[13].

Figure 9 shows the simulation results for the case of a R=12 guide star and a turbulence strength of r_0 =12.8 cm. The simulation parameters are summarized in Table 4.

Figure 9(a) shows the time histories of the piston-removed segment WFE computed directly from the residual phase screens. Note that a WFE level of less than 200 nm RMS is reached very fast as soon as the AO loop closes. The segment WFE improves gradually as the MGM converges, reaching a final value of ~120 nm RMS.

The MGM starts to operate at $t = 0.5$ s. The OGC coefficients are initialized to $\{\mathscr{k}_i\}$=1, and the modal gains of the OMGI controller are initialized to $\{g_i\}$=0.5. Figure 9(e) and (f) illustrate the convergence of the OGTL. Note that it takes ~5 iterations to converge (i.e. the effective optical gains of the probes stabilize at $\gamma_i^{eff} \approx 1$). The OMGI gains after convergence are shown in Figure 10.

Table 4. Summary of the NGAO simulation parameters.

Telescope: ▪ GMT pupil area: 358 m^2 **Atmospheric Turbulence:** ▪ 7 layers median profile for Las Campanas Observatory ▪ r_0 = 12.8 cm ▪ L_0= 25 m ▪ τ_0= 3.0 ms **NGAO control loop:** ▪ 500 segment KL modes / segment ▪ Frame rate: 1 kHz ▪ Total loop delay: 2 frames **Modal Gain Machine:** ▪ Update rate: 1 Hz ▪ $g_{OGTL} = 0.5$	**Guide star:** ▪ R-magnitude: 12 ▪ Spectral flux distribution: top-hat **Throughput:** ▪ Telescope (M1,M2,M3): 0.729 ▪ Instrument window: 0.9 ▪ NGWS common path: 0.4 ▪ PWFS / HDFS light split: 0.9 / 0.1 **Pyramid WFS:** ▪ Integration time: 1 ms ▪ 92×92 sub-apertures ▪ Modulation: $\pm 2\lambda_1/D$ ▪ EMCCD: RON 0.5 e- RMS ▪ $g_{EMCCD} = 600$ ▪ $g_{ADU} = 1/30$ ▪ Zero point: 9×10^{12} ph/s ▪ Expected photons/SA/frame: 6	**HDFS:** ▪ Integration time: 150 ms ▪ EMCCD: RON 0.5 e- RMS ▪ $g_{EMCCD} = 600$ ▪ $g_{ADU} = 1/30$ ▪ Zero point: 6.6×10^{12} ph/s ▪ Expected photons/SA/frame in diff.-limited conditions: ~10000

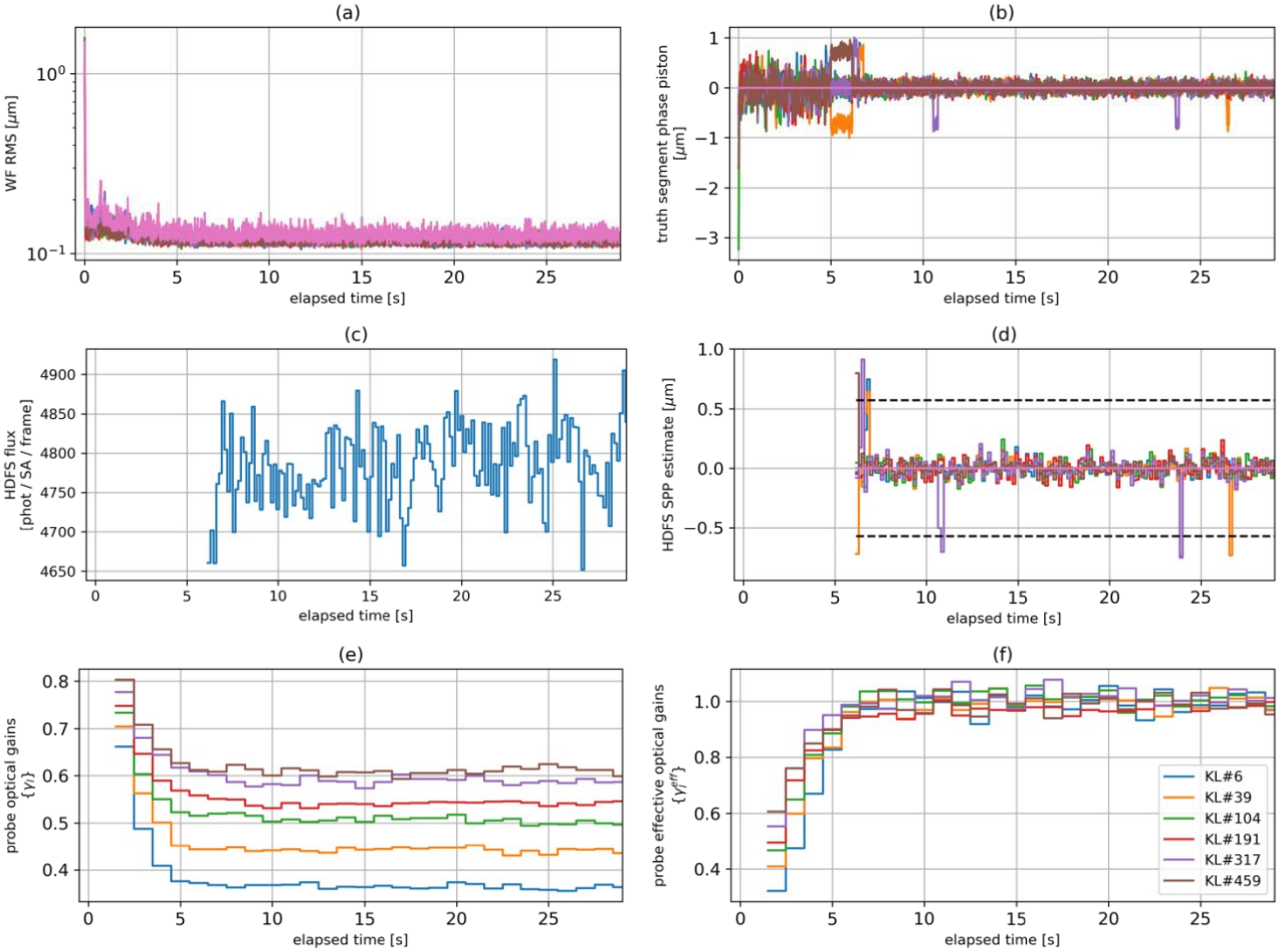

Figure 9. Simulation results for a mR=12 guide star and r_0 =12.8 cm **(a)** piston-removed WFE over each segment. **(b)** Truth segment phase piston. **(c)** HDFS flux level. **(d)** HDFS segment phase piston estimate. The detection thresholds are also shown. **(e)** Probe optical gains. **(f)** Probe effective optical gains.

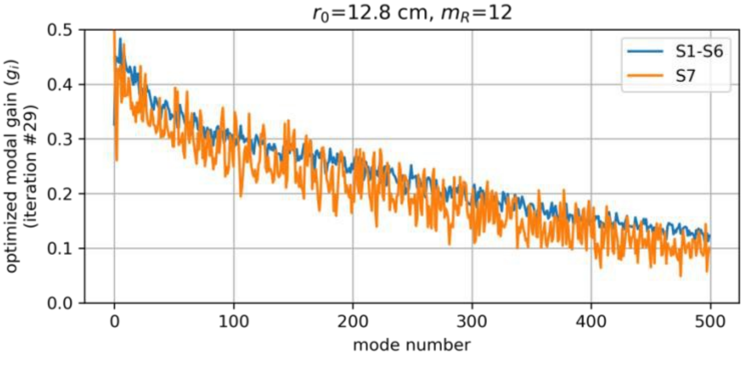

Figure 10. Optimized Modal Gains determined by the MGM for the simulated observing conditions.

Figure 9(b) shows the time histories of the segment phase pistons (w.r.t the central segment) computed directly from the residual phase screens. Segment piston ejections almost always occur when first closing the loop (even when starting with a perfectly phased telescope like in this simulation). To minimize the amplitude of ejections (i.e. the number of waves) we first close the AO loop controlling all modes except segment piston with the feedback of the PWFS. Segment piston commands during this bootstrapping stage ($0 < t < 5$ s) are computed using the turbulence covariance matrices between the rest of the segment KL modes (here referred to as high-order modes) and segment piston modes:

$$m_p(n) = C_{ph} C_{hh}^{-1} m_h(n) \tag{11}$$

where C_{hh} is the von-Karman covariance matrix of high-order modes; C_{ph} is the von-Karman covariance matrix between high-order and segment piston modes; m_h denotes the high-order modal command vector, and m_p denotes the segment piston vector. The covariance matrices are pre-computed numerically by projecting a large number of turbulence phase screens onto the segment KL modes.

The control of segment piston modes using the feedback of the PWFS should start after the convergence of the MGM (at t=5 s in this simulation). Note that a first estimate of the OGC coefficients for segment piston modes is available at this time too. As shown in Figure 9(b), once the PWFS takes control there are a couple of segments stabilized at one wave that need to be recovered by the HDFS.

The HDFS start operation at $t = 6.0$ s. The HDFS flux level and segment piston estimates are shown in Figure 9(c) and (d) respectively. Note that the HDFS average flux/SA/frame is ~4800 photons, which is considerably lower than the flux estimated in diffraction-limited conditions, due to the action of the HDFS spatial filter.

A zoom in of the segment piston time histories around $t = 6.0$ s is shown in Figure 11(a). The HDFS recovers the two ejected segments in one iteration ($t = 6.15$ s), but there are still segment ejections immediately after, since the optimized modal gains for segment piston are still not found by the MGM.

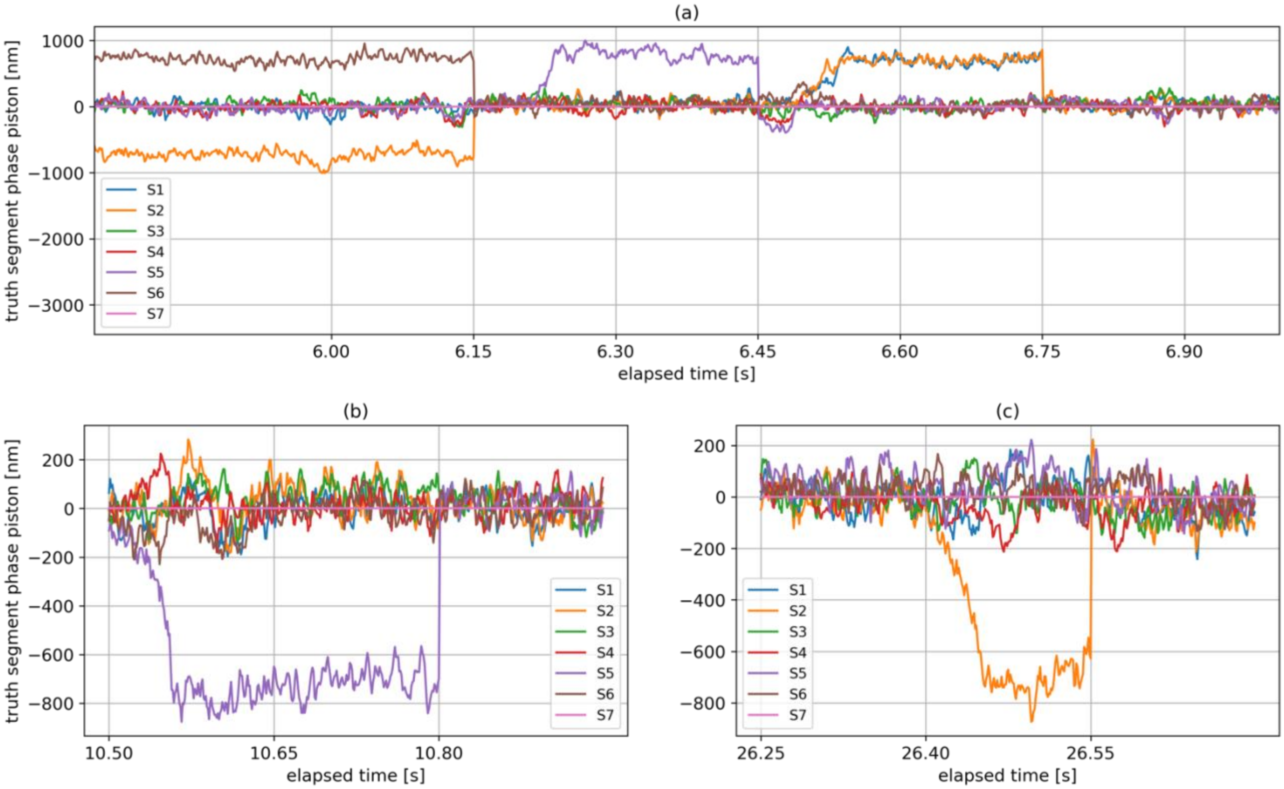

Figure 11. Truth segment phase piston at selected locations where phase-wrapping errors occurred. **(a)** Zoom in around the time the HDFS started operation (t = 6s). **(b)** Zoom in about $t = 10.50$ s where a segment ejection of S5 occurred. **(c)** Zoom in about $t = 26.40$ s where a segment ejection of S2 occurred.

In steady-state operation segment ejections may still occur, as shown in Figure 9(b). A zoom in around the time of two of these ejection occurrences are shown in Figure 11(b) and (c). Note that the HDFS is effective in recovering these ejections. An example of HDFS fringes under the realistic simulated conditions are shown in Figure 12.

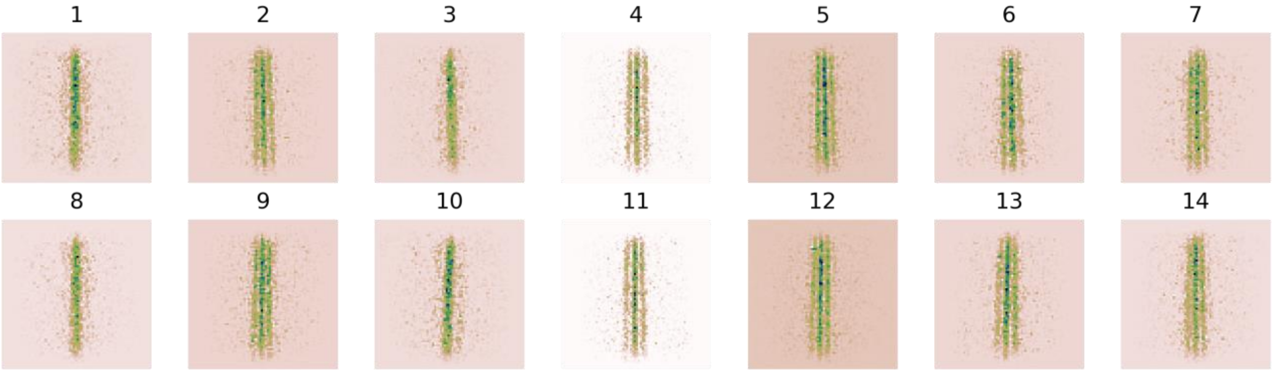

Figure 12. HDFS fringes at first iteration ($t = 6.15$ s), detecting the ejections of S1 and S6 segments.

5. SUMMARY AND FUTURE WORK

In this paper we have presented an optimized modal control strategy that has allowed us to reduce the frequency and amplitude of segment ejections caused by phase-wrapping errors of the pyramid WFS. We have also presented a bootstrapping strategy making use of statistical priors on the turbulence to control segment piston while waiting for the Modal Gain Machine to converge. The adoption of the Holographic Dispersed Fringe Sensor (HDFS) as 2nd NGWS channel for segment piston sensing has improved the recovery efficiency. The HDFS interferes full segment pupils, instead of only a small area across the gap like the AGWS DFS[7,8]. This provides a significant gain in sensitivity in an AO-corrected regime.

We have presented simulation results under a specific observing condition (R=12, r_0 =12.8 cm). The performance evaluation and parameter optimization under lower GS flux and worse seeing conditions is under way. We should note that we are currently implementing a full regularized reconstruction and pseudo-open loop control (POLC) that will further improve the performance under those conditions.

Finally, we are planning to test the NGAO control strategy using the PWFS+HDFS architecture on the High Contrast AO Phasing Testbed (HCAT) under development at the University of Arizona[14].

ACKNOWLEDGMENTS

This work has been supported by the GMTO Corporation, a non-profit organization operated on behalf of an international consortium of universities and institutions: Arizona State University, Astronomy Australia Ltd, the Australian National University, the Carnegie Institution for Science, Harvard University, the Korea Astronomy and Space Science Institute, the São Paulo Research Foundation, the Smithsonian Institution, the University of Texas at Austin, Texas A&M University, the University of Arizona, the University of Chicago, and the Weizmann Institute of Science.

S.Y.H. is supported by NASA through the NASA Hubble Fellowship grant #HST-HF2-51436.001-A awarded by the Space Telescope Science Institute, which is operated by the Association of Universities for Research in Astronomy, Incorporated, under NASA contract NAS5-26555.

REFERENCES

[1] Fanson, J. L., Bernstein, R., Ashby, D., Bigelow, B. C., Brossus, G., Burgett, W. S., et al., “Overview and status of the Giant Magellan Telescope project”, Proc. SPIE 12182, 12182-45 (2022).

[2] Bouchez, A. H., Conan, R., Demers, R. T., McLeod, B. A., Quirós-Pacheco, F., et al., "Overview and status of the GMT wavefront control system", Proc. SPIE 12185, 12185-48 (2022).

[3] Millan-Gabet, R., Bernstein, R., Souza, A., Walls, B., Bouchez, A., et al., "Science instrumentation progress at the Giant Magellan Telescope", Proc. SPIE 12814, 12814-68 (2022).

[4] Pinna, E., Agapito, G., Quirós-Pacheco, F., Antichi, J., Carbonaro, L., Briguglio, R., et al., "Design and numerical simulations of the GMT Natural Guide star WFS", Proc. SPIE 9148, 91482M (2014).

[5] Haffert, S. Y., Close, L. M., Hedglen, A. D., Males, J. R., Kautz, M., et al., "Phasing the Giant Magellan Telescope with the holographic dispersed fringe sensor", J. Astron. Telesc. Instrum. Syst. 8(2) 021513 (2022).

[6] Agapito, G., Rossi, F., Plantet, C., Puglisi, A., and Pinna, E., "Advances in control of a pyramid single conjugate adaptive optics system", MNRAS 508, 1745–1755 (2021).

[7] van Dam, M. A., McLeod, B. A., Bouchez, A. H., "Dispersed fringe sensor for the Giant Magellan Telescope", Applied Optics Vol. 55, No. 3 (2016).

[8] Kopon, D. A., and McLeod, B. A., "On-sky results of the next generation GMT phasing sensor prototype", Proc. SPIE 10703, 10703-34 (2018).

[9] Esposito, S., Puglisi, A., Pinna, E., Agapito, G., Quirós-Pacheco, F., Verán, J.-P., and Herriot, G., "On-sky correction of non-common path aberration with the pyramid wavefront sensor", A&A 636, A88 (2020).

[10] Veran, J.-P., and Herriot, G., "Centroid gain compensation in a Shack-Hartmann adaptive optics system: implementation issues", Proc. SPIE 4007 (2000). doi: 10.1117/12.390349

[11] Dessenne, C., Madec, P.-Y., and Rousset, G., "Optimization of a predictive controller for closed-loop adaptive optics", Applied Optics Vol. 37, No. 21 (1998).

[12] Conan, R., Bouchez, A., Quirós-Pacheco, F., and McLeod, B., "The GMT Dynamic Optical Simulation", AO4ELT4 Conference Proceedings (2015). http://dx.doi.org/10.20353/K3T4CP1131598

[13] Okuta, R., Unno, Y., Nishino, D., Hido, S., and Loomis, C., "CuPy: A NumPy-Compatible Library for NVIDIA GPU Calculations", *Proceedings of Workshop on Machine Learning Systems (LearningSys) in The Thirty-first Annual Conference on Neural Information Processing Systems (NIPS)*, (2017).

[14] Hedglen, A. D., Close, L. M., Haffert, S. Y., Males, J. R., Kautz, M. Y., et al., "Lab tests of segment/petal phasing with a pyramid wavefront sensor and a holographic dispersed fringe sensor in turbulence with the Giant Magellan Telescope high contrast adaptive optics phasing testbed", J. Astron. Telesc. Instrum. Syst. 8(2) 021515 (2022).